Electronic Supplementary Material (ESI) for Physical Chemistry Chemical Physics.

SUPPORTING INFORMATION

Photo-Induced Heat Generation in Non-Plasmonic Nanoantennas

Stefano Danesi,[a,b] Marco Gandolfi,[c,d] Luca Carletti,[e] Nicolò Bontempi,[f] Costantino De Angelis,[f,g]

Francesco Banfi,[c] Ivano Alessandri[a,f, g]*

*[a]INSTM-UdR Brescia, via Branze 38, 2513 Brescia, Italy; [b] Department of Mechanical and Industrial Engineering, via Branze 38, 2513 Brescia, Italy; [c]Interdisciplinary Laboratories for Advanced Materials Physics (I-LAMP), via Musei 41, 25121 Brescia, Italy; [d] Dipartimento di Matematica e Fisica, Università Cattolica del Sacro Cuore, Via Musei 41, 25121 Brescia, Italy; [e] Laboratory of Soft Matter and Biophysics, Department of Physics and Astronomy, KU Leuven, Celestijnenlaan 200D, B-3001 Leuven, Belgium; [f] Department of Information Engineering, University of Brescia, via Branze 38, 2513 Brescia, Italy; [g] INO-CNR, via Branze 38, 2513 Brescia, Italy.*e-mail: ivano.alessandri@unibs.it*

S1. The model

The model developed for the simulations encompasses both optical and thermal properties of the core/shell systems and the Si crystal substrate. Thus, the computational strategy was based on the sequential solution of both the electromagnetic (EM) and thermal problems. The first problem was addressed by calculating the EM field in all the positions of the domain. This field was subsequently used to calculate the generated Joule heating, that was then introduced into the Fourier steady state equation as heat source. Here we considered the EM absorption as the only source of heat.

In Figure SI1 the domain model, already shown in the main text, is replicated for convenience. The EM problem was solved on a much smaller domain defined in proximity of the core-shell structure (Figure SI1), while the thermal problem was solved on a real size domain. This choice is dictated by the heavy computational load involved in solving Maxwell's equations. The EM domain includes the core-shell system, a substrate portion of 40 nm depth and an air portion, which is above (blow-up of Figure SI1). Lateral dimensions are limited by a cylindrical border of radius $3.5 \times w_0$, being w_0 the exciting radiation beam waist. The thermal domain consists in a 7 mm x 7 mm x 0.5 mm substrate, the core sphere of 230 nm in diameter and the shell layer with thickness, h, between 10 nm and 100 nm.

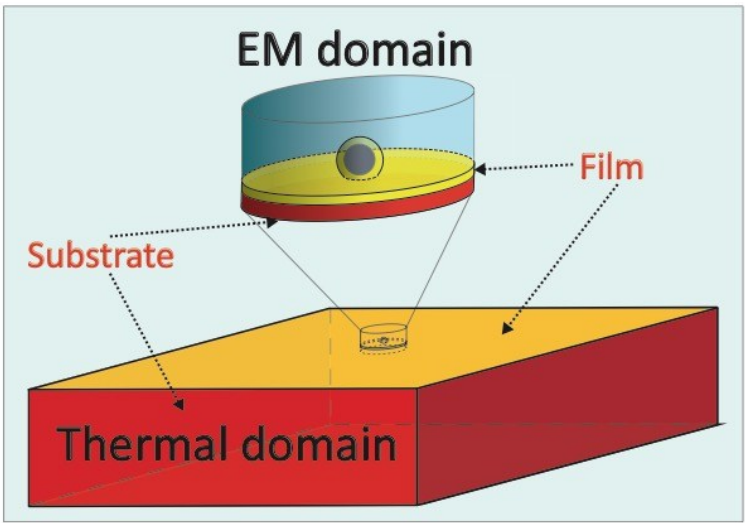

Figure S1.1 Thermal and EM domain (blow-up) utilised for solving the Fourier and Maxwell's equation respectively. The EM domain is much narrower respect to the thermal one, but this does not affect the temperature estimation.

The incoming light was modelled as a laser focused by a 100X (0.9 numerical aperture, NA) microscope objective. Equation (1) shows the relation between the beam waist w_0 and the vacuum radiation wavelength (λ_0) under the aforementioned focalization conditions:

$$w_0 = \frac{\lambda_0}{\pi \times NA} \qquad (1)$$

The focus was located in the centre of the core sphere. We note that no difference was found by moving the focus through the core/shell sphere. Second order scattering boundary conditions were applied on all the EM boundary surfaces to reproduce open boundaries.

For non-magnetic materials, the heat generated by EM absorption is given by:

$$Q_e = \frac{1}{2}\varepsilon_0 Re\left\{\frac{\omega\varepsilon''(\omega)}{4\pi}E \cdot E^*\right\} \qquad (2)$$

where E is the complex electric field, and ε'' is the imaginary part of the relative dielectric permeability .

The values of the relative dielectric permittivity used in the simulations are summarized in Table S1

	c-Si	a-Si	SiO_2
ε_r (λ=532 nm)	17.237+0.430 i [1]	18.830+7.770 i [2]	2.176+$1 \cdot 10^{-5}$ i [3,4]
ε_r (λ=633 nm)	15.072+0.152 i [1]	17.512+3.547 i [2]	2.167+$1 \cdot 10^{-5}$ i [3,4]
ε_r (λ=785 nm)	13.734+0.054 i [1]	15.322+0.981 i [2]	2.159+ $1 \cdot 10^{-5}$ i [3,4]

Table S1. Values of the complex dielectric function at three different wavelengths for c-Si, a-Si and SiO_2.

Light to heat conversion in air was considered negligible, being ε'' and μ'' equal to zero. Once that the portion of electromagnetic energy converted in heat was obtained, the steady-state heat diffusion equation:

$$\nabla \cdot (k(r,T,h)\nabla T(r)) + Q_e(r) = 0 \qquad (3)$$

where $k(r,T,h)$ is the thermal conductivity and $T(r)$ is the absolute temperature field was used. To obtain $T(r)$ in all the points of the system, the non-linear differential equation (3) is solved, and boundary conditions were applied, to account for convection, radiative dissipation and Kapitza resistance.[12]

The convection contribution to heat dissipation was accounted by applying on all the air-exposed boundaries the condition:

$$q_c \cdot n = h_c(T_{ext} - T) \quad (4)$$

where q_c is the convective heat flux, n is a versor normal to the surface and h_c is the heat transfer coefficient, whose expressions was taken from references [6-11].[6-11] T and T_{ext} are respectively the system and the external absolute equilibrium temperatures, with T_{ext} kept fixed at the room temperature $293.15\ K$.

The radiative thermal dissipation contribution has been considered by imposing Stefan-Boltzmann equation on all the air exposed surface.

$$q_r \cdot n = A\ \sigma\ \varepsilon\left(T^4 - T_{ext}^4\right) \quad (5)$$

where q_r is the radiative heat flux, A the area of the exposed surface, σ is the Stefan-Boltzmann constant, ε the surface emissivity. For a-Si $\varepsilon = 0.9$, for c-Si $\varepsilon = 0.7$ and for SiO_2 $\varepsilon = 0.8$.

At the SiO_2/c-Si, SiO_2/a-Si and c-Si/a-Si interface, a Kapitza resistance value of $1 \cdot 10^{-9}\ m^2K/W$ was set.[12, 17]

The radiative heat transfer by means of surface-to-surface radiation is negligible due to the absence of closely interfaced surfaces.[5]

The a-Si thermal conductivity (*see* note S.1.4) was set at 1.8 $W/m \cdot K$.[16] Its value is independent on temperature and film thickness. The thermal conductivity of c-Si, instead, strongly depends on temperature and film thickness h. Considering the bulk temperature dependence[13] $k_T(T)$ and

the thermal conductivity accumulation function[14] $\alpha_{\%}(h)$ for the size dependence,[14,15] an expression for $k(T,h)$ was obtained:

$$k(T,h) = k_T(T) \times \alpha_{\%}(h) \qquad (6)$$

The calculated thermal conductivity can vary from 150 $W/m \cdot K$ for bulk c-Si at room temperature to less than 1 $W/m \cdot K$ for a shell thickness of 10 nm at temperature higher than 700 K. The thermal conductivity accumulation function is defined as the ratio $k(h)/k_{\infty}$ between its value computed for a simulation cell with thickness h and its corresponding extrapolated value for a bulk-like sample. $\alpha_{\%}(h)$ gives the contribution to the thermal conductivity provided by phonons with mean free path up to h.

As a consequence of the EM domain truncation, the heat source term does not extend all over the thermal domain, like in the real case. In order to account for the neglected heat, an equivalent 2D source is set in the thermal domain on a surface corresponding to the boundaries of the EM substrate domain. The source value in each point of the boundary was set equal to the time averaged Poynting vector magnitude evaluated in that point. It has been verified that such approximation overestimate the system's maximum temperature of a value lower than 10 K. When such a power source is neglected, or temperature is set equal to the external equilibrium temperature (273.15 K), the temperature is heavily underestimated.

Additional notes:

1) Influence of the contact point size in the calculation of ΔT_{max}.

The value of ΔT_{max} depends on the value of the contact area between the sphere and the substrate. Figure S1.2 shows the trend of ΔT_{max} values as a function of the contact area,

calculated either under resonant (film thickness: 75 nm, red curve) and non-resonant (film thickness: 50 nm, black curve) conditions for a generic nanoantenna. The contact area utilized in the present work (1000 nm^2), corresponding to a radius of 17.8 nm, is indicated by the red mark. We note that the contact area can be either increased or decreased down to about 250 nm^2 without any significant variation of ΔT_{max}. On the other hand, under resonant conditions, these values increases up to 1600 K when the contact area tends to zero. Thus the contact radius utilized in the present work (17.8 nm) represents a reliable choice to simulate the maximum temperature variations over a wide range of contact angle values. The high temperature variations resulting under efficient opto-thermal coupling conditions have been confirmed also from experimental data reported in reference 24 of the main text.

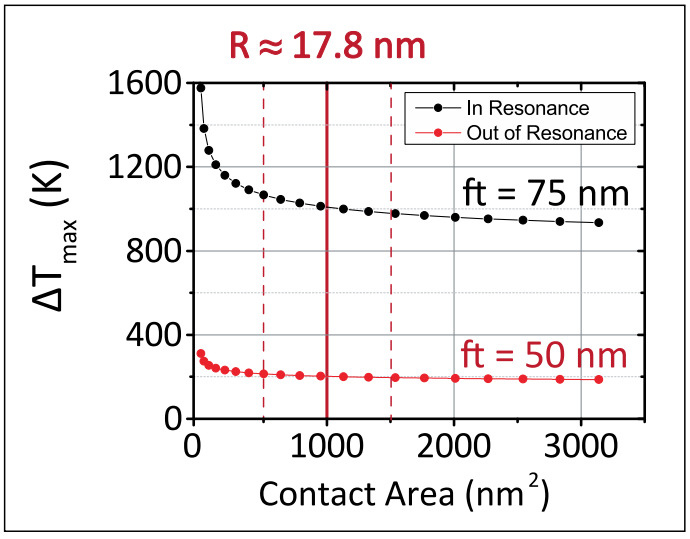

Figure S1.2. ΔT_{max} *vs.* contact area, calculated either under resonant (film thickness: 75 nm, red curve) and non-resonant (film thickness: 50 nm, black curve) conditions for generic non-conformal nanoshells. The contact area utilized in the present work is indicated by the red mark.

2) Influence of air thermal conductivity

As most of the Raman experiments on core/shell spheres are carried out in air (in general a few droplets of an analyte in solution are drop-casted on the spheres and dried before Raman acquisition), the contribution of air thermal conductivity should be taken into account. However, the numerical calculations reported in the present work have been performed without considering the contribution of air thermal conductivity. Figure S1.3 shows that this approximation has a negligible effect on the simulations. This is justified by the fact that thermal conductivity in air ranges between 0.026 W/(mK) and 0.1 W/(mK) in the temperature interval considered in the numerical calculations, thus air is a good insulator and cannot efficiently dissipate the photo-generated heat. A detailed study on the opto-thermal behaviour of the spheres in water is in progress and will be addressed in future works.

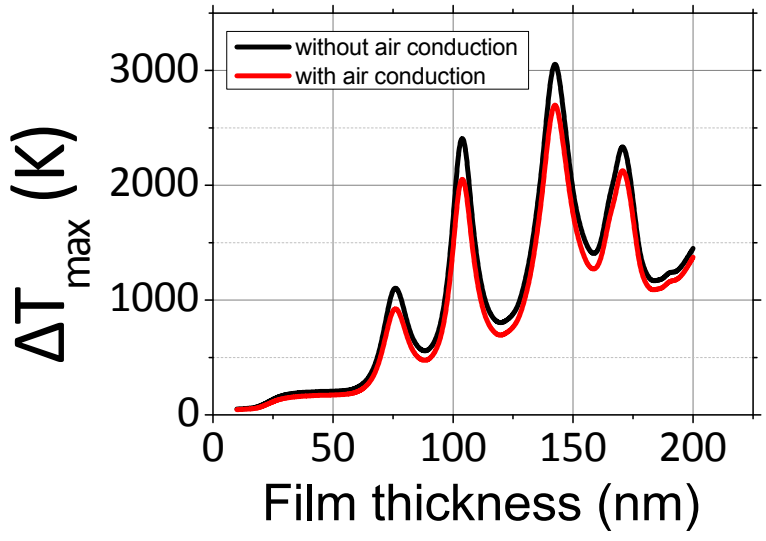

Figure S1.3. Example of the effects of air thermal conductivity on the results of numerical simulations (*see* also paragraph S3 for details on the system simulated in this case).

3) Calculation of the absorption cross section

The absorption cross section has been obtained by the following equation:

$$\sigma_{Abs} = \int_{Vol} \frac{Q_e}{S_{in}} dV$$

where

$$Q_e = \frac{1}{2}\varepsilon_0 \frac{\omega \varepsilon''(\omega)}{4\pi} Re\{E \cdot E^*\} \left[\frac{W}{m^3}\right]$$

is the power absorbed by the core-shell structure, and

$$S_{in} = \frac{|E|^2}{2 \cdot Z_0} \left[\frac{W}{m^2}\right]$$

represents the incident power density.

E is the electric field vector and is distributed in space as a focalized Gaussian beam.

Z_0 is the free space impedance.

4) Dependence of thermal conductivity on size

The main effects of material's size impact on the choice of the thermodynamic parameters. A detailed explanation of the values utilized in the present work and the criteria at the basis of their choice are detailed below.

1) **a-Si:** the thermal conductivity used in this work is 1.8 W/(m*K) and is temperature-invariant. Experimental evidences reported in reference 16 (SI) have been used as reference for the determination of such a value. In the latter work, the thermal conductivity of films with thickness values that are lower or comparable to those utilized in our simulations were determined in a temperature range spanning from 30 to 750 K. No significant variations with size and temperature were observed.

2) c-Si: In this work the dependence of thermal conductivity on the film thickness has been accounted by taking the work of Melis *et. al.* (ref. 15 SI) as a main reference. In this work, the authors utilized a molecular dynamics computation technique to calculate the film thickness dependence of thermal conductivity. The final result gives an accumulation function that, multiplied for the bulk value gives the thermal conductivity for every film thickness. In addition, the dependence of thermal conductivity on temperature has been taken into account (*see* Figure S1.4 (a)). The overall thermal conductivity has been calculated as the product of the bulk temperature dependent value times the accumulation function.

3) SiO_2: the value used for thermal conductivity is the bulk value because no less than 20 nm sized structures has been employed in our work. The temperature dependence of thermal conductivity is shown in Figure S1.4 (b).

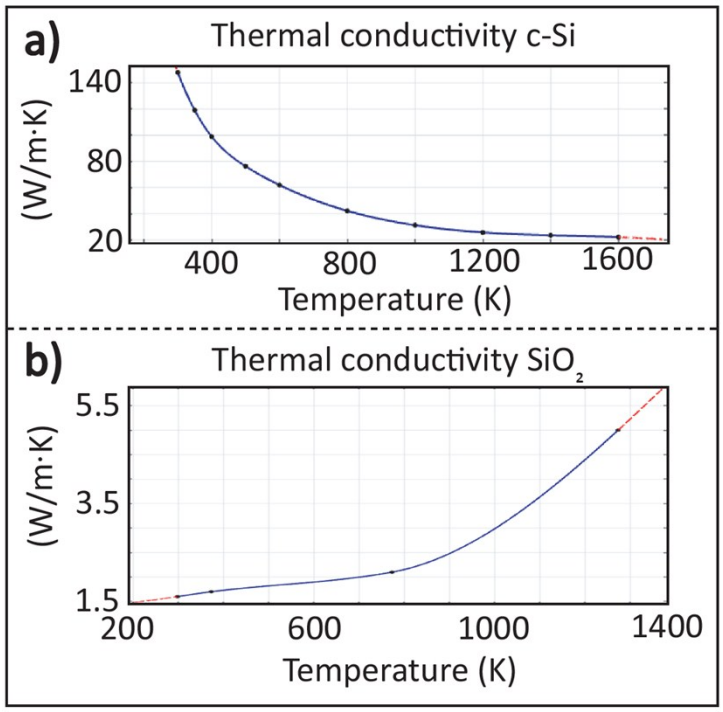

Figure S1.4. Thermal conductivity as a function of the temperature of the system for a) c-Si and b) SiO_2.

All those aspects further highlight the nonlinear nature of heat equations. This is one of the reasons behind the choice of Finite Elements Analysis to treat these systems.

S2. Threshold power calculation at λ= 532, 633 and 785 nm

The threshold power, *i.e.* the power required to reach the bulk melting temperature of either a- or c-Si, was calculated for three different exciting laser wavelengths (532, 633 and 785 nm). Given the nonlinear relation between temperature and exciting power, a special algorithm was developed to find the threshold value, using COMSOL Multiphysics Livelink for Matlab Mathworks.

The algorithm was based on the following steps:

1. The system was excited with a low test power (P) and consequently the maximum temperature over the geometry $T_{max}(P)$ was computed and compared with the shell's melting temperature T_{thr}.
2. If $T_{max}(P) < T_{thr}$ the test power was increased and step 1 was repeated. This step was repeated until two powers $P_1$and P_2differing by less than 2 mW were not found, so that $T_{max}(P_1) < T_{thr}$ and $T_{max}(P_2) > T_{thr}$.
3. The power corresponding to the melting temperature was found by making a linear interpolation between $P_1$and P_2.
4. A check was done by setting the approximated threshold power as an input in the model. In all the cases, the resulting maximum temperature was less than 5 K away from the respective melting values.

The threshold power as a function of film thickness for the conformal and non-conformal

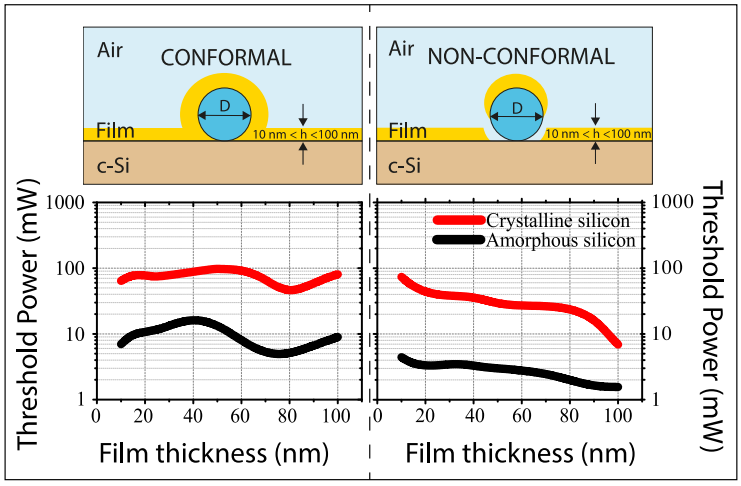

a-and c-Si cases are shown in Figures S2.1 and S2.2 for λ=633 and λ=785 nm, respectively. The calculations at λ=532 nm are shown and discussed in the main text.

Figure S2.1. Threshold power as a function of film thickness, for (a) conformal and (b) non-conformal core-shell systems. The red lines refer to c-Si while the black lines refer to a-Si shells. The irradiation by a C.W. laser at λ=633 nm was simulated.

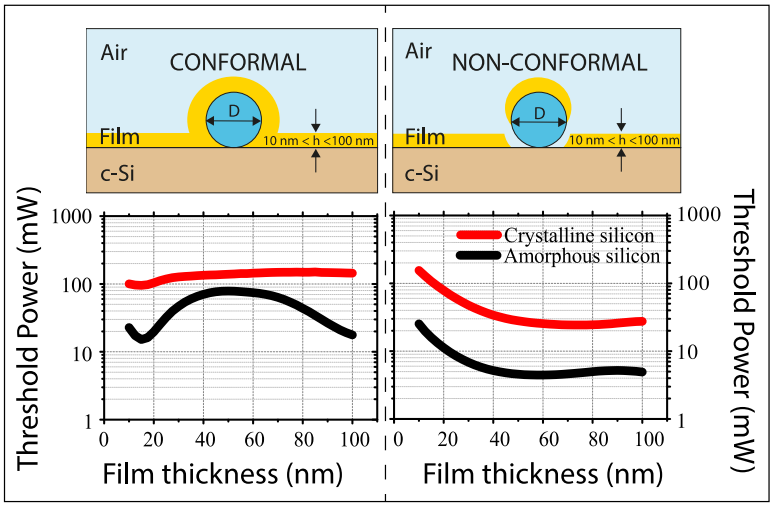

Figure S2.2 Threshold power as a function of film thickness, for (a) conformal and (b) non-conformal core-shell systems. The red lines refer to c-Si while the black lines refer to a-Si shells. The irradiation by a C.W. laser at λ=785 nm was simulated.

S3. Extended simulation for c-Si nanoshells (thickness range: 10-200 nm)

For the c-Si nanoshell excited at λ=532 (red dashed line in Figure 3d in the main text) the optical absorption curve is shown only up to film thicknesses of 100 nm where a sudden increase is observed, suggesting the presence of optical resonances for thicker shells. To proof this hypothesis we extended the simulation range up to 200 nm-thick shells (Figure S3). However, we note that those resonances are associated to temperature values that exceed the melting threshold of Si, thus they cannot be exploited for Raman sensing purposes but could be very efficient local heaters.

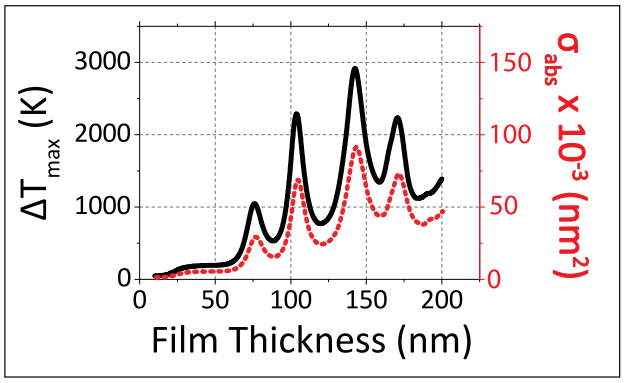

Figure S3. Maximum temperature shift (black line) and absorption cross-section (dashed red line) of the c-Si non-conformal nanoshells in 10-200 nm thickness range (λ=532 nm, power: 1.25 mW).

S4. F.E. *vs.* ΔT at λ= 532, 633 and 785 nm: Figures of Merit

Figure S4 shows the figures of merit (FOM) calculated from the ratio between field enhancement (F.E.) and temperature enhancement (ΔT): FOM=FE/ΔT. By contrasting F.E. to ΔT, each FOM allows a rapid evaluation of the potential use (either Raman sensing or local heating) of a specific nanoshell irradiated at given wavelength. We note that the figure of merit decreases as the laser wavelength decreases. The system behaves like a good heat generator at short wavelength and as a good field enhancer at higher wavelengths. Moreover, the crystalline

systems generally offer better field enhancement performances, except in correspondence of resonances, where the figure of merit decays.

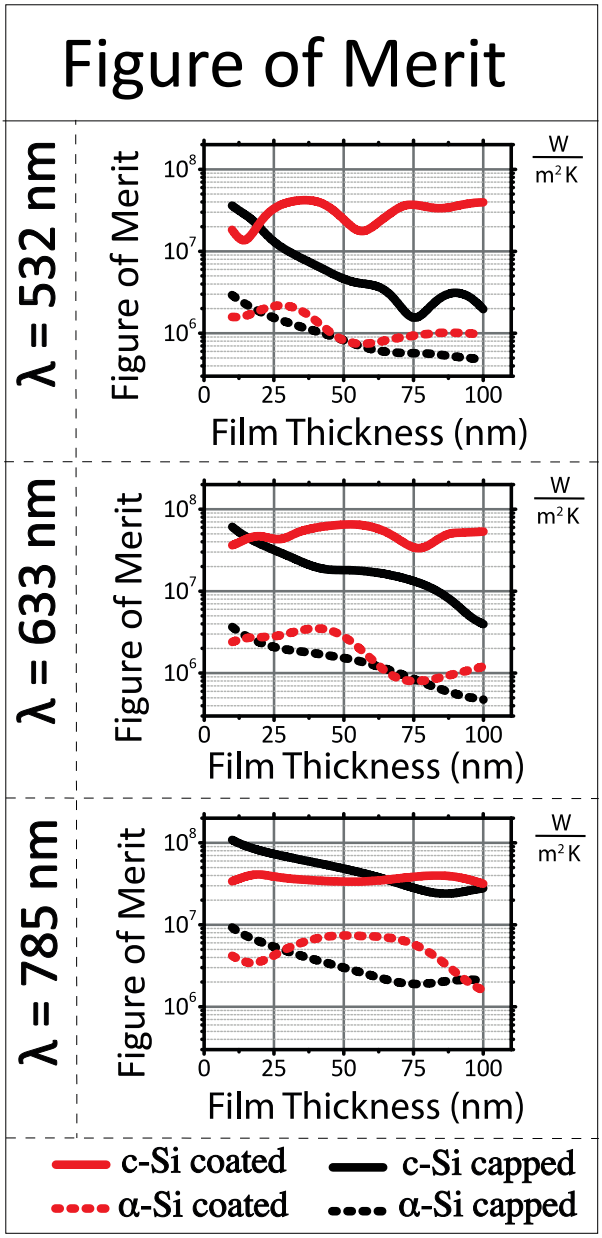

Figure S4. Figure of merit obtained at λ=532 nm, 633 nm, 785 nm and for an incident power of 1.25 mW.

S5. REFERENCES

1) Aspnes, D. E.; Studna, A. A. Dielectric Functions and Optical Parameters of Si, Ge, GaP, GaAs, GaSb, InP, InAs, and InSb from 1.5 to 6.0 eV. *Phys. Rev. B*, **1983**, *27*, 985-1009.

2) Palik, E. D. *Handbook of Optical Constants of Solids*, Academic Press: Boston, MA, 1985.

3) Gao, L.; Lemarchand, F.; Lequime, M. Exploitation of Multiple Incidences Spectrometric Measurements for Thin Film Reverse Engineering. *Opt. Express,* **2012,** *20*, 15734-15751.

4) Alessandri, I.; Lombardi, J. R. Enhanced Raman Scattering with Dielectrics. *Chem. Rev.* **2016**, *116*, 14921–14981.

5) St-Gelais, R.; Zhu, L.; Fan, S.; Lipson, M. Near-field radiative heat transfer between parallel structures in the deep subwavelength regime. *Nature Nanotech.* **2016**, *11*, 515-519.

6) Lloyd, J. R.; Moran, W. R. Natural Convection Adjacent to Horizontal Surface of Various Planforms, *J. Heat Transfer* **1974**, *96*, 443-447.

7) Goldstein, R. J.; Sparrow, E. M.; Jones, D. C. Natural Convection Mass Transfer Adjacent to Horizontal Plates. *Int. J. Heat Mass Tran* **1973***, 16*, 1025-1035.

8) Churchill, S. W.; Humbert, H.S.; Correlating Equations for Laminar and Turbulent Free Convection From a Vertical Plate, *Int. J. Heat Mass Tran* **1975**, *18*, 1323-1329.

9) Schulenberg, T. Natural Convection Heat Transfer Below Downward Facing Horizontal Surfaces, *Int. J. Heat Mass Tran* **1985**, *28*, 467-477.

10) Churchill, S.W. Free Convection around Immersed Bodies, *Heat Exchanger Design Handbook*, Hemisphere Publishing, New York, 1983.

11) Thornton, S. T.; Rex, F. A. *Modern Physics for Scientists and Engineers*, Saunders College Publishing, 1993.

12) Chen, J.; Zhang, G.; Li, B. Thermal Contact Resistance Across Nanoscale Silicon Dioxide and Silicon Interface. *J. Appl. Phys.,* **2012**, *112*, 064319.

13) Touloukian, Y. S.; Powell, R. W.; Ho, C. Y.; Klemens, P. G. Thermal Conductivity: Nonmetallic Solids, *Thermophysical Properties of Matter – The TPRC Data Series*, IFI/Plenum Data Corp., New York, 1970.

14) He, Y.; Savić, I.; Donadio, D.; Galli, G. Lattice Thermal Conductivity of Semiconducting Bulk Materials: Atomistic Simulations. Phys. Chem. Chem. Phys. **2012**, *14*, 16209-16222.

15) Melis, C.; Dettori, R.; Vandermeuled, S.; Colombo, L. Calculated Thermal Conductivity in a Transient Conduction Regime: Theory and Implementation. *Eur. Phys J. B*, **2014**, 87, 96 (1-9).

16) S. Moon, M. Hatano, M. Lee, C. P. Grigoropulos, Thermal conductivity of amorphous silicon thin films. *Int. J. Of Heat and Mass Transfer* **2002**, 45, 2439-2447.

17) Lanord, A. F.; Blandre, E.; Albaret, T.; Merabia, S.; Lacroix, D.; Termentzidis, K. Atomistic Amorphous/Crystalline Interface Modelling for Superlattices and Core/Shell Nanowires. *J. Phys. Condens. Matter*, **2014**, *26,* 355801.